Hindawi Publishing Corporation
International Journal of Photoenergy
Volume 2015, Article ID 213858, 10 pages
http://dx.doi.org/10.1155/2015/213858

Research Article

Sb_2S_3 Quantum-Dot Sensitized Solar Cells with Silicon Nanowire Photoelectrode

You-Da Hsieh,[1] Ming-Way Lee,[2] and Gou-Jen Wang[1,3]

[1]*Department of Mechanical Engineering, National Chung-Hsing University, Taichung 40227, Taiwan*
[2]*Department of Physics, National Chung-Hsing University, Taichung 40227, Taiwan*
[3]*Graduate Institute of Biomedical Engineering, National Chung-Hsing University, Taichung 40227, Taiwan*

Correspondence should be addressed to Gou-Jen Wang; gjwang@dragon.nchu.edu.tw

Received 31 December 2014; Revised 11 March 2015; Accepted 11 March 2015

Academic Editor: Leonardo Palmisano

We propose a novel quantum-dot sensitized solar cell (QDSSC) structure that employs a quantum dot/semiconductor silicon (QD/Si) coaxial nanorod array to replace the conventional dye/TiO_2/TCO photoelectrode. We replaced the backlight input mode with top-side illumination and used a quantum dot to replace dye as the light-absorbing material. Photon-excited photoelectrons can be effectively transported to each silicon nanorod and conveyed to the counter electrode. We use two-stage metal-assisted etching (MAE) to fabricate the micro-nano hybrid structure on a silicon substrate. We then use the chemical bath deposition (CBD) method to synthesize a Sb_2S_3 quantum dot on the surface of each silicon nanorod to form the photoelectrode for the quantum dot/semiconductor silicon coaxial nanorod array. We use a xenon lamp to simulate AM 1.5 G (1000 W/m^2) sunlight. Then, we investigate the influence of different silicon nanorod arrays and CBD deposition times on the photoelectric conversion efficiency. When an NH (N-type with high resistance) silicon substrate is used, the QD/Si coaxial nanorod array synthesized by three runs of Sb_2S_3 deposition shows the highest photoelectric conversion efficiency of 0.253%. The corresponding short-circuit current density, open-circuit voltage, and fill factor are 5.19 mA/cm^2, 0.24 V, and 20.33%, respectively.

1. Introduction

In general, the dye-sensitized solar cell (DSSC) is categorized, with respect to its components, as an organic compound solar cell. The DSSC is the only organic compound solar cell that utilizes molecules to absorb photons and converts photons into electrons without relying on the intermolecular transfer of the excited electrons. The DSSC is also the only solar cell type that conducts light harvesting and charge-carrier transport functions at different places [1]. Compared to the conventional silicon-based solar cell, the main advantages of the DSSC include its simple manufacturing process, low cost, physical and chemical TiO_2 stability, lack of toxicity, and wider application range. Although the photoelectric conversion efficiency of the DSSC has not reached the level of silicon-based solar cells, a DSSC with an efficiency of 12.3% has been reported [2].

Although the fabrication of DSSCs is relatively simple and cost-effective, mass production of DSSCs is still limited for a number of reasons. The main issue is the aging of the dye during solar cell operation. In addition, most of the available dyes can only absorb photons within the visible light range. Furthermore, the commonly used photoelectrode is based on the coating and the successive sintering of TiO_2 on a fluorine-doped tin oxide (FTO) glass to obtain an anatase type of TiO_2. The sintering of TiO_2 not only degrades the conductivity of the FTO substrate but also limits mass production fabrication. Recently, semiconductor-sensitized solar cells (SSSCs) that use semiconductors to replace the dye have attracted attention. Since the activity of a semiconductor will not degrade during solar cell operation, theoretically, the lifetime of an SSSC should be much longer than that of the conventional DSSC.

The quantum-dot sensitized solar cell (QDSSC) is one kind of DSSC [3–9]. Different semiconductor quantum dots (QDs) are used to replace dye as the light absorber. In addition to the lifetime enhancement of the light absorbers, the photon absorption range can be accurately manipulated

by selecting the type and size of the QD. Hence the photon absorption range can be greatly expanded by combining several types of QDs that absorb photons of various wave lengths. A QDSSC using a CdS/CdSe hybrid QD with a photoelectric conversion efficiency of 4.22% was reported in 2009 [5]. Later, another QDSSC with a better photoelectric conversion efficiency (6.5%) was developed [8]. Shalom et al. [10] used a DSSC consisting of a photoelectrode by directly depositing QDs onto an FTO glass to quantify the lifetime and density of the photogenerated electrons within the QD layer. The authors verified that the electronic properties in quantum dot-sensitized solar cells are illumination intensity-dependent. Buhbut et al. [11] deposited type-II ZnSe/CdS colloidal core/shell QDs on top of a standard CdS QD sensitizer layer to enhance the open-circuit voltage (V_{oc}). They demonstrated that the extent of the additional photovoltage is a function of the illumination intensity. Kumar et al. [12] reported the development of a new photoactive electrode, made by assembling lead sulfide (PbS) and cadmium sulfide (CdS) QDs and functionalized graphite platelets (FGPs) onto TiO_2, with a photoelectric conversion efficiency of 3.82%, which is 54% higher than that of the TiO_2/CdS DSSC.

Nanomaterials and nanofabrication techniques have also been incorporated into the fabrication of DSSCs to achieve higher efficiency and lower cost [13–15]. The nanostructured photoelectrode can support the electrolyte and the dyes, as well as the acceptor and the conductor of the photoexcited electrons. A porous nanostructured photoelectrode can provide the electrolyte and the dyes with a sufficient absorption area to achieve a fast charge transfer. Hence the photoelectric conversion efficiency can be enhanced.

In this study, we propose a novel and simple QDSSC structure using a silicon nanowire array (SNA) as the substrate. We use chemical bath deposition (CBD) [16–18] to grow Sb_2S_3 QDs between the silicon nanowires to form the QD/Si coaxial nanowire array, replacing the conventional dye/TiO_2/TCO photoelectrode. The photon-excited photoelectrons from the Sb_2S_3 QDs can be effectively transported to each silicon nanorod and then conveyed to the counter electrode. Since the silicon substrate is not fully transparent, we adapted illumination from the counter electrode. We expected that the high-surface-to-volume Si nanowire array would greatly expand the absorption area of the $Sb2S_3$ QDs, hence increasing efficiency. Furthermore, the proposed new DSSC structure can be easily and directly produced in a silicon wafer, making the mass production of the proposed QDSSC highly feasible.

2. Material and Methods

2.1. QD/Si Coaxial Nanowire Array-Based DSSC. Figure 1 schematically illustrates a cross-sectional view of the proposed QD/Si coaxial nanowire array-based QDSSC. Solar light irradiates through the counter electrode and then penetrates the electrolyte to the photoelectrode of the QD/Si coaxial nanowire array to produce photoelectrochemical reactions. The photon-excited electrons are conveyed from the QD shell to the Si nanowire core and then are driven to the counter electrode through the back electrode, finally entering the electrolyte and reducing the ions therein. The QDs that have loose electrons due to photoelectrochemical reactions retrieve the electrons provided by the oxidation reactions in the electrolyte.

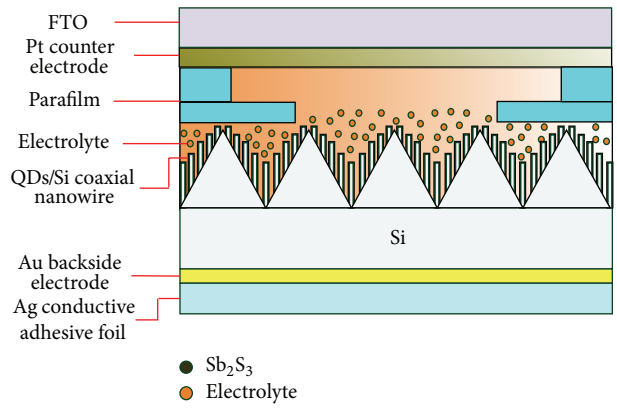

Figure 1: Schematic of the proposed QD/Si coaxial nanowire array-based QDSSC.

2.2. Fabrication of the Silicon Nanowire Photoelectrode Based Sb_2S_3 QDSSC. The fabrication procedures of the proposed novel QDSSC include (1) Si nanowire array fabrication, (2) Sb_2S_3 QDs deposition, (3) metal electrode fabrication, (4) counter electrode preparation, (5) electrolyte preparation, and (6) cell packaging as schematically illustrated in Scheme 1.

(1) Si Nanowire Array (SNA) Fabrication. In this study, we adopted an upright 3-dimensional SNA that grew on a pyramid array, in order to allow more QDs to adhere to the SNA. We employed the metal-assisted etching (MAE) method to fabricate the SNA [19–21]. In this study, we used 4-inch N-type Si wafers with a thickness and resistivity of 200 μm and 1–3 Ω-cm (Wafer Works, Taiwan), respectively, as the substrate for SNA fabrication. For the etchant in the MAE process, we used a mixture of silver nitrate ($AgNO_3$) and hydrofluoric acid (HF). The Si substrate provides electrons to the silver atoms to reduce the silver ions in the etchant, which then cover the surface of the silicon substrate. At the same time, the silicon ions are oxidized to SiO_2, which is then dissolved by the HF solution without any externally applied potential. A Si nanowire array can thus be produced through successive reduction and oxidation (redox) reactions.

We used a two-stage MAE to enable the fabrication of a uniform SNA [22, 23]. First, we conducted a short-time MAE using a high-concentration $AgNO_3$ to produce a silver layer on the surface of the KOH-etched micropyramid array. Next, we executed a relatively long-time MAE using a lower concentration of $AgNO_3$ to grow an upright and uniform SNA on the surface of the micropyramid. The fabrication procedures are briefly described as follows.

(i) Wafer cleaning: wash the Si wafer in acetone, ethanol (EtOH), and distilled water sequentially and

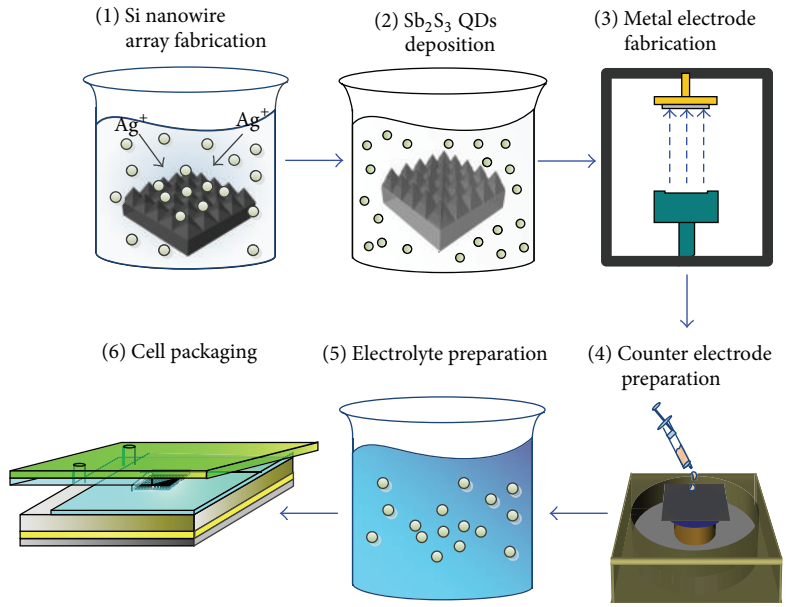

Scheme 1: QDSSC fabrication procedures.

ultrasonically, and then remove the oxide layer on the wafer surface with diluted HF acid. Then, wash the wafer with distilled water.

(ii) Micropyramid array production: wet-etch the cleaned Si wafer using an etchant with a weight ratio of DI water: KOH (40 wt%): IPA = 70 : 2 : 5 to create the micropyramid array on the wafer surface. Then, use more dilute HF acid to remove the oxide layer from the wafer surface.

(iii) Two-stage MAE: for the first MAE stage, use a mixing etchant of $AgNO_3$ (0.34 M) and HF (4.6 M) at 40°C for 30 min. Then, for the second MAE stage use $AgNO_3$ (0.03 M) and HF (4.6 M) mixing etchant at 40°C for 5 min. Remove the silver conifers that accumulate on the nanowire surface during the MAE process using nitric acid (HNO_3). Finally, remove the SiO_2 layer produced during the previous silver conifer removal step using an HF and distilled water mixing solution (ratio = 1 : 3).

(2) Sb_2S_3 QDs Deposition. We employed the chemical bath deposition (CBD) method to deposit a QD shell of Sb_2S_3 on each individual Si nanowire, thereby establishing the QD/Si coaxial nanowire array photoelectrode. The steps we followed in this method are detailed below.

(i) $Na_2S_2O_3$ solution preparation: dissolve the $Na_2S_2O_3 \cdot 5H_2O$ (6.2 g) with 25 mL distilled water, followed by 10 min of ultrasonication to obtain a transparent solution with no precipitate.

(ii) $SbCl_3$ solution preparation: take the $SbCl_3$ (0.65 g) from the nitrogen glove box and dissolve it in 2.5 mL ethanol. Ultrasonicate this solution for 10 min to obtain a transparent solution with no precipitate.

(iii) Sb_2S_3 QDs deposition: pour the prepared $Na_2S_2O_3$ and $Na_2S_2O_3$ solution into a beaker and use distilled water at 5°C to increase the total volume of the CBD solution to 100 mL. Observe white suspensions that are the products of the $SbCl_3$-water chemical reactions. Transfer the CBD solution to a specific bottle for CBD. Then shake the bottle to allow uniform chemical reactions, followed by vertically immersing the prepared SNA specimen into the bottle. Keep the CBD bottle at 5°C for 2 h per cycle and shake the bottle every half hour to ensure a uniform distribution of the solution. Then take the SNA specimen out of the bottle and rinse it with distilled water to obtain an orange amorphous Sb_2S_3 layer on the SNA surface. Finally, anneal the QDs-covered SNA specimen at 350°C for 30 min, increasing the temperature from room temperature to 350°C in 20 min.

(3) Metal Electrode Fabrication. Since the SNA substrate is a semiconductor, it must sputter a 30 nm thick thin gold film electrode on the bottom side of the substrate to reduce the series resistance of the DSSC and form ohmic contact, thereby enhancing the carrier collection capacity of the photoelectrode.

(4) Counter Electrode Preparation. Platinum thin film was used as the counter electrode material. The preparation procedures of the Pt counter electrode are briefly summarized below.

(i) Punch two small holes in a commercially available FTO substrate. One is used for the injection of the electrolyte, and the other one is used to exhaust the air inside the cell during the electrolyte injection process. Wash the FTO substrate in acetone, ethanol (EtOH),

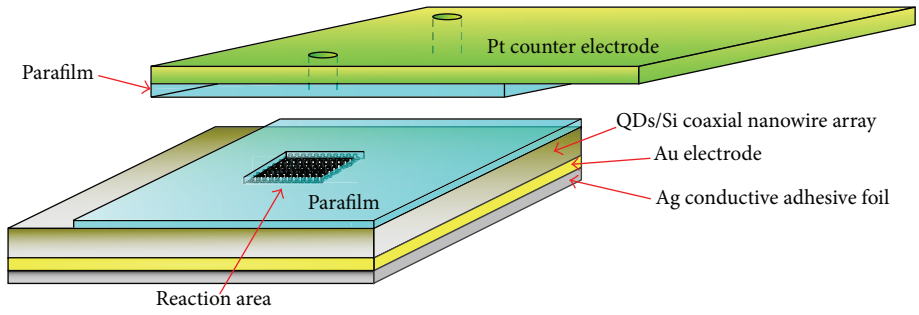

Figure 2: Schematic of the cell packaging procedures.

and distilled water sequentially and ultrasonically, followed by heating at 60°C for 20 min to completely remove residual moisture.

(ii) Prepare a 5 mM H_2PtCl_6 solution by mixing 0.0515 g of H_2PtCl_6 with 20 mL ethanol, followed by ultrasonication for 10 min. Spin-coat the H_2PtCl_6 solution onto the cleaned FTO substrate twice. The rotational speed and duration for each coating are 1000 rpm and 10 min, respectively. Finally, sinter the H_2PtCl_6 solution-coated FTO at 400°C for 15 min to obtain the Pt thin film counter electrode.

(5) Electrolyte Preparation. The electrolyte used in the DSSCs must have a high diffusion coefficient, a fast oxidation-reduction reaction, and a low intrinsic resistance. The formula for the electrolyte used in this study that satisfies these requirements is

$$0.5\,\text{M LiI} + 0.05\,\text{M I2} + 0.5\,\text{M TBP} + 0.6\,\text{M BMII in Acetonitrile} + \text{Valeronitrile}\ (1:1). \quad (1)$$

(6) Cell Packaging. The cell packaging procedures, as illustrated in the schematic in Figure 2, are as follows.

(i) Prepare a $1.5 \times 1.5\,\text{cm}^2$ rectangular parafilm. Punch a $0.3 \times 0.3\,\text{cm}^2$ square in the center of the rectangular parafilm as the photoreaction area.

(ii) Prepare a $1.5 \times 1.5\,\text{cm}^2$ rectangular parafilm. Punch a $0.5 \times 0.5\,\text{cm}^2$ square in the center of the rectangular parafilm as the buffer for the electrolyte leakage.

(iii) Attach the parafilm with the defined buffer square to the Pt thin film counter electrode, and then attach them both to the photoelectrode.

(iv) Bond the packaged device at 85°C for 7 min. It may be desirable to place an external load on top to ensure solid bonding of the parafilms.

(v) Adhere a silver conductive adhesive foil to the Au thin film electrode beneath the photoelectrode for clamping the measurement fixture.

(vi) Inject the electrolyte into the cell body using a syringe.

3. Results and Discussion

3.1. SNA Fabrication Results. After the fabrication of the SNA on the surface of the pyramid array using the two-stage MAE process, we then deposited Sb_2S_3 QDs on the surface of each of the SNA nanowires to serve as the photoelectrode. Since the relatively high-concentration $AgNO_3$ etchant used in the first stage contained more silver ions, the reduced silver atoms aggregated at the surface of the Si substrate and were uniformly deposited on the Si substrate. However, the Si substrate could also be oxidized quickly by the highly concentrated silver ions; therefore, the processing time of the first-stage MAE was set to be less than 1 min. The low-concentration $AgNO_3$ etchant used in the second-stage MAE enabled the uniformly deposited silver particles on the substrate surface to etch downward slowly so that a uniform SNA, microscale in height, could be fabricated.

Figure 3 shows SEM images of the fabricated SNA under a constant first-stage processing time of 30 sec and various second-stage processing times. We can observe that Si nanowires with heights of micrometers grew uniformly on the surface of the pyramid array. We also found that the length of the SNA increased with an increased second-stage processing time. The top-view image, as shown in the inset in each image, displays the Si nanowires on the surface of the pyramid array.

In successive experiments, we set the second-stage processing time at 5 min, accompanied by various first-stage processing times (20, 25, 30, 35, 40, and 45 sec). Figure 4 illustrates the fabrication results. The SNAs fabricated under first-stage processing times of 20 and 25 sec (Figures 4(a) and 4(b)) reveal denser but shorter structures. We speculate that the shorter first-stage processing time produced smaller silver particles, resulting in an unevenly distributed redox reaction speed in the second stage of the MAE process. In Figures 4(c) and 4(d), uniform and vertical SNAs with micrometer lengths can be observed. The SNAs fabricated with a relatively longer first-stage processing time (Figures 4(e) and 4(f)) have a relatively looser and more flexible structure. These results can be mainly attributed to the fact that a longer first-stage processing time induces a continuous catalytic reaction on the substrate surface.

3.2. QDs Sb_2S_3 Characterization. The novelty of this study is the development of the photoelectrode with the QD/Si

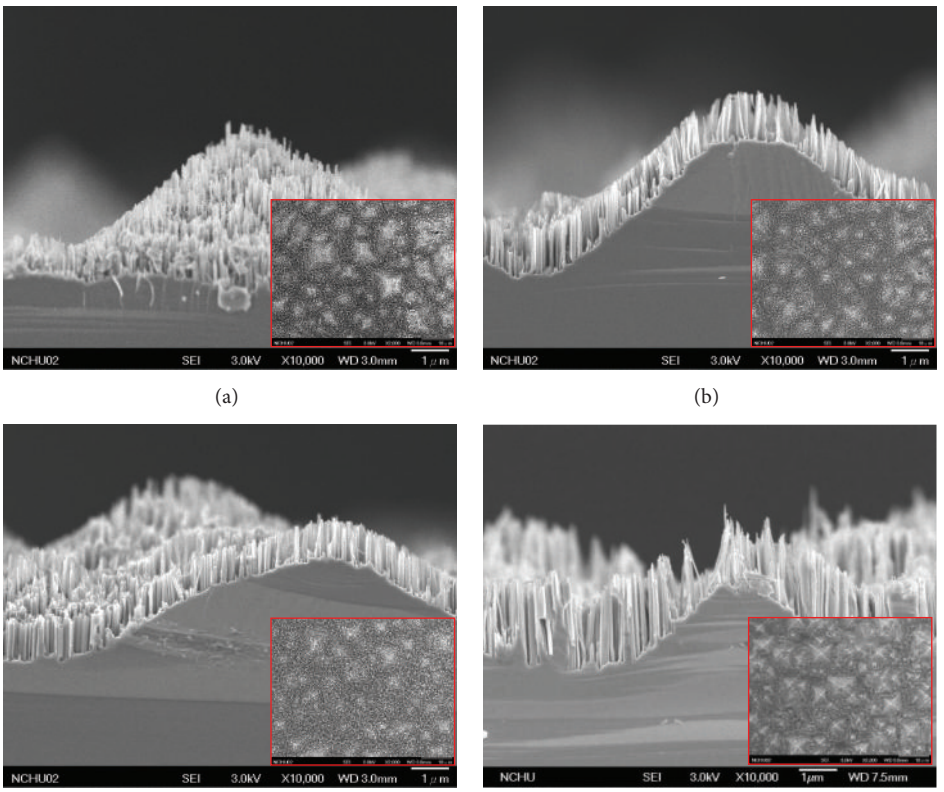

FIGURE 3: SEM images of the fabricated SNA under a constant first-stage processing time of 30 sec and various second-stage processing times: (a) second-stage processing time: 1 min, (b) 2 min, (c) 3 min, and (d) 4 min.

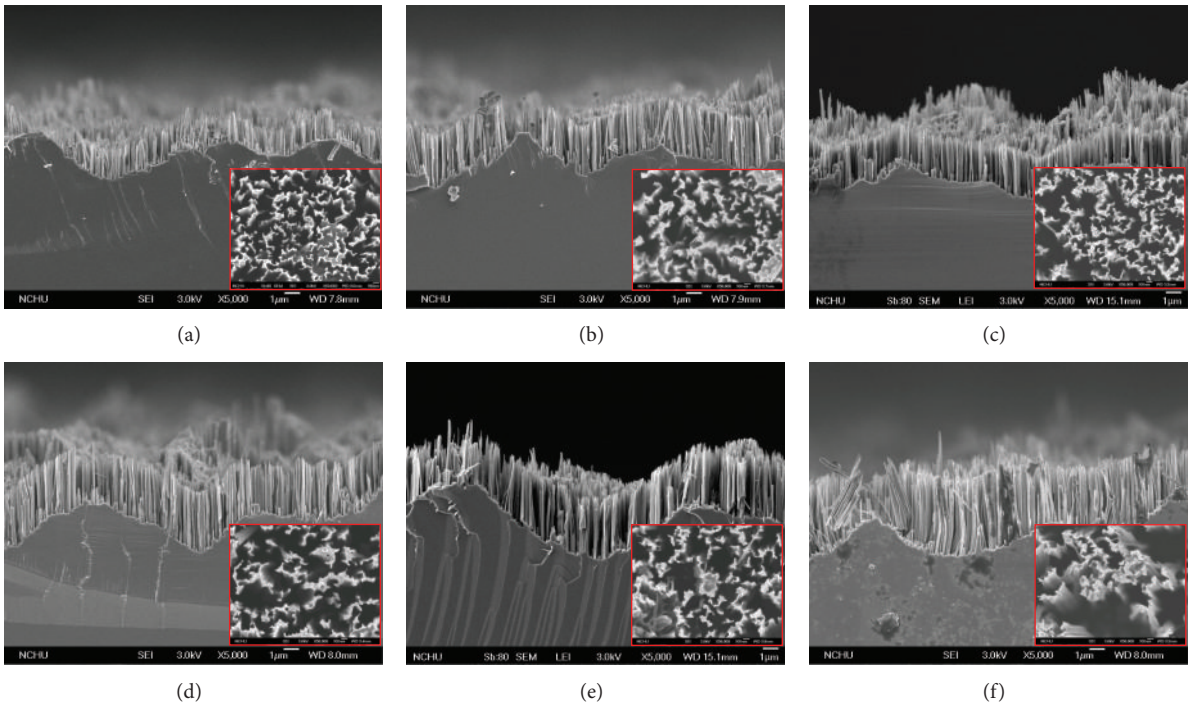

FIGURE 4: SEM images of the fabricated SNA under a constant second-stage processing time of 5 min and various first-stage processing times: (a) first-stage processing time: 20 sec, (b) 25 sec, (c) 30 sec, (d) 35 sec, (e) 40 sec, and (f) 45 sec.

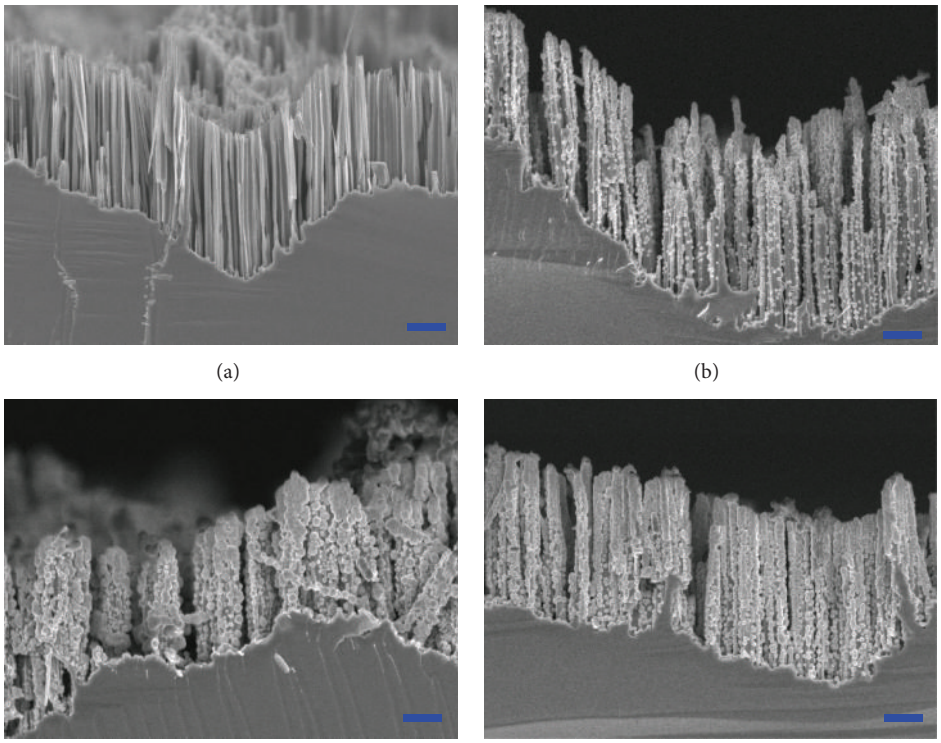

(a) (b)

(c) (d)

Figure 5: SEM images for the synthesized QD/Si coaxial nanowire array after various CBD cycles: (a) 1 CBD cycle, (b) 2 CBD cycles, (c) 3 CBD cycles, and (d) 4 CBD cycles. Scale bar = 1 μm.

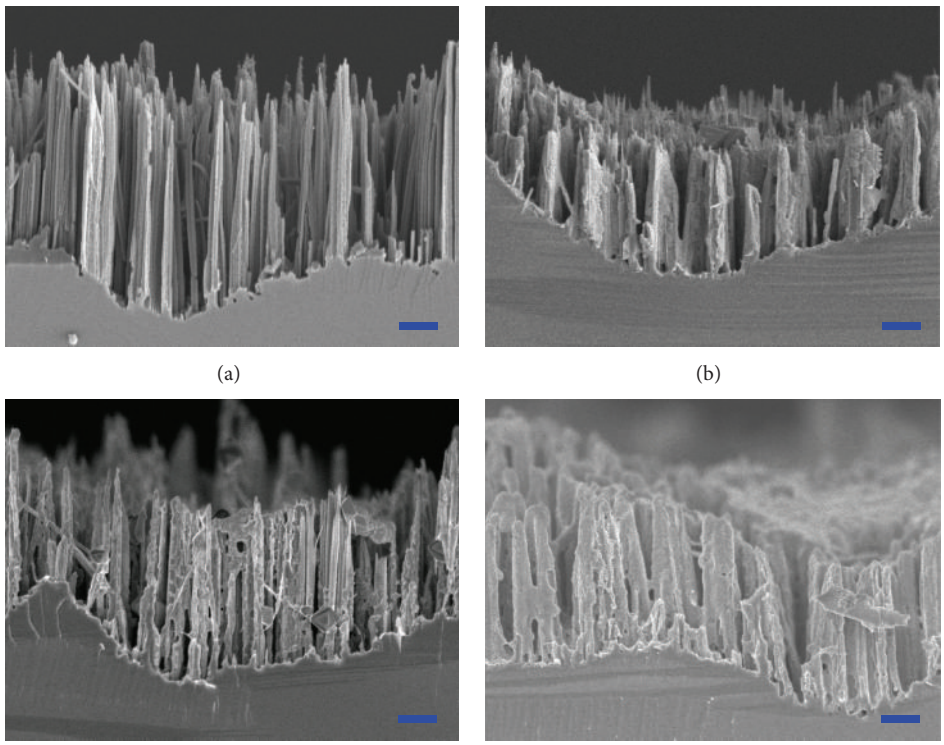

(a) (b)

(c) (d)

Figure 6: SEM images after annealing of the QD/Si coaxial nanowire array for various CBD cycles: (a) 1 CBD cycle, (b) 2 CBD cycles, (c) 3 CBD cycles, and (d) 4 CBD cycles. Scale bar = 1 μm.

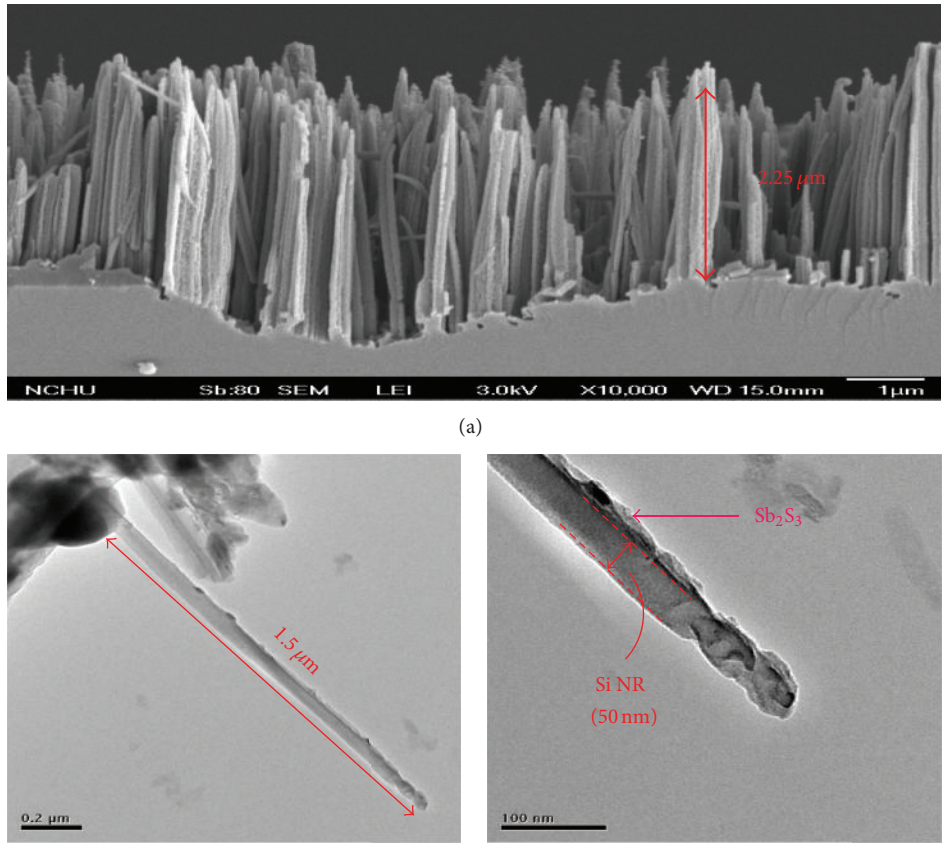

Figure 7: Images of the synthesized coaxial nanowire arrays after 1 CBD cycle: (a) cross-sectional SEM image, (b) TEM (×12,000), and (c) TEM (×40,000).

coaxial nanowire array. The properties of the synthesized Sb_2S_3 surrounding each nanowire highly affect the performance of the DSSC. Therefore, we used scanning electron microscopy (SEM), energy dispersive spectroscopy (EDS), and transmission electron microscopy (TEM) to characterize the synthesized Sb_2S_3 QDs.

(1) Topography Analysis. SEM images for the QD/Si coaxial nanowire array for various CBD cycles are shown in Figures 5 and 6. Figure 5 displays the synthesized coaxial nanowire array, while Figure 6 presents array images after annealing. Figures 5(a) and 6(a) are the images before and after annealling of the coaxial nanowire arrays after 1 CBD cycle. We find no apparent difference between these two arrays but for several plush-like structures at the tip of the array after annealing (Figure 6(a)). The array images before and after annealing after 2 CBD cycles are shown in Figures 5(b) and 6(b), respectively. Compared with the images of the 1 CBD cycle arrays, relatively more obvious topographical differences can now be observed. More nanoparticles are attached to the surface of each nanowire in Figure 5(b). After annealing, the attached nanoparticles disappeared and each nanowire was covered by a film which enlarged the size of the nanowire. When the number of CBD cycles was increased to three, each nanowire was fully surrounded by nanoparticles after the CBD process (Figure 5(c)). After annealing, the topography was similar to that shown in Figure 6(b). Besides the tip of the nanowire, the rest of the nanowire either was fully covered by a thin film or adhered to neighboring nanowires, forming the desired photoelectrode with a QD/Si coaxial nanowire array (Figure 6(c)). Figures 5(d) and 6(d) show images of the nanowire arrays after 4 CBD cycles. Each Si nanowire was completely covered by Sb_2S_3 nanoparticles after the CBD process. After annealing, no obvious shape of the original nanowire can be seen. The photoelectrode with distinct QD/Si coaxial nanowires can be seen in Figure 6(d).

The above SEM analyses indicate that the Sb_2S_3 nanoparticles started to adhere to the nanowire surface after 2 CBD cycles and fully covered each nanowire when the number of CBD cycles was increased to four. We therefore suggest that the CBD process should be repeated 2–4 times to obtain the desired QD/Si coaxial nanowire array-based photoelectrode.

(2) Components Analysis. To further verify that both the nanoparticles and the thin film covering the Si nanowire after annealing consist of Sb_2S_3, we conducted an EDS analysis. Table 1 tabulates the components of the coaxial nanowire array fabricated under different CBD cycles. We can observe that the samples contain antimony (Sb) and sulfur (S), which are the components of Sb_2S_3. The data indicate that

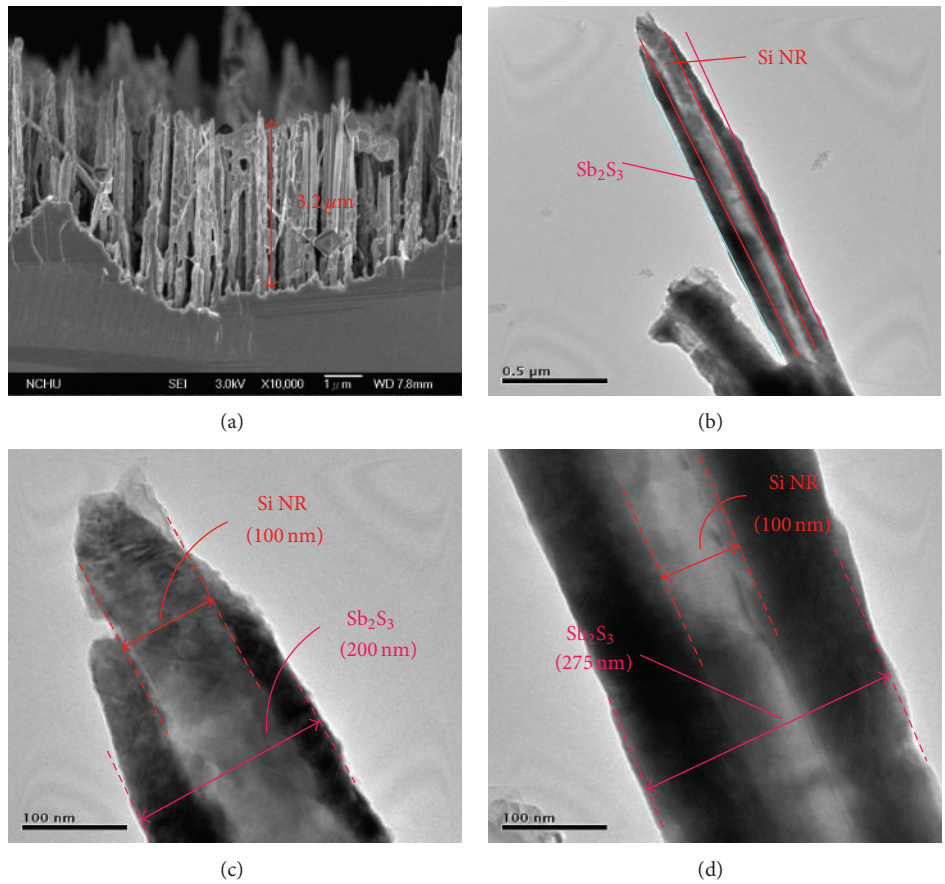

Figure 8: Images of the synthesized coaxial nanowire arrays after 3 CBD cycles; (a) cross-sectional SEM image, (b) individual coaxial nanowire TEM (×8,000) image, (c) front end TEM (×40,000) image, and (d) middle TEM (×40,000) image.

Table 1: Components of the coaxial nanowire array fabricated after different numbers of CBD cycles.

CBD cycles	Si (Weight%) (Atomic%)	S (Weight%) (Atomic%)	Sb (Weight%) (Atomic%)
0	88.24	4.04	7.73
	94.32	3.78	1.90
1	45.93	14.70	39.37
	67.66	18.96	13.38
2	32.52	18.81	48.66
	54.00	27.36	18.64
3	14.97	23.55	61.47
	30.07	41.44	28.49
4	9.94	22.35	67.71
	22.03	43.37	34.60

the percentage of Sb_2S_3 in the samples increased with an increased number of CBD cycles. In contrast, the percentage of Si gradually decreased.

(3) Structure Analysis. Figures 7 and 8 show images of the synthesized coaxial nanowire arrays after 1 and 3 CBD cycles, respectively. The SEM image shown in Figure 7(a) indicates that the length of the coaxial nanowire array is around 2.25 μm. The length of the individual nanowire shown in the TEM image (Figure 7(b)) is 1.5 μm, which is close to the entire array length indicated by the SEM image. Figure 7(c) displays the ×40,000 magnified image. Clear boundaries separating the core Si nanowire and the coated Sb_2S_3 can be observed. The diameter of the core Si nanowire is estimated to be 50 nm. Similarly, the length of the 3-CBD-cycle-synthesized coaxial nanowire array, as shown in Figure 8(a), is about 3.2 μm. An individual coaxial nanowire, as shown in Figure 8(b), measures 2 μm in length. Boundaries separating the core Si nanowire and the Sb_2S_3 coating are more apparent in this figure. At the front end, the diameters of the core Si nanowire and the coaxial nanowire are estimated to be 100 and 200 nm, respectively (Figure 8(c)). In the middle, the diameter of the core Si nanowire remained at 100 nm, while that of the coaxial nanowire increased to 275 nm (Figure 8(d)). The cause of the size difference at the front end and the middle can be attributed to the downward flow of the Sb_2S_3 QDs during annealing.

Table 2 summarizes the TEM analysis results for various QDs/Si coaxial nanowire arrays fabricated with different numbers of CBD cycles. Since the TEM sample was prepared by supersonicating the synthesized photoelectrode sample in

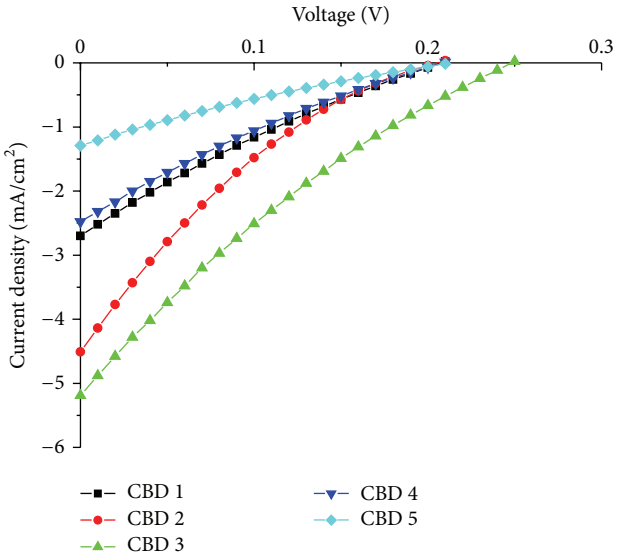

Figure 9: *I-V* curves for various DSSCs based on the QDs/Si coaxial nanowire array-based photoelectrodes synthesized with different numbers of CBD cycles.

Table 2: TEM analysis results for various QDs/Si coaxial nanowire arrays fabricated with different numbers of CBD cycles.

CBD cycles	Si nanowire diameter (nm)	Sb_2S_3 shell thickness (nm)
1	50	20
2	60	30
3	100	50 (front), 87.5 (middle)
4	80	195 (front), 225 (middle)

an alcohol solution for 2 h and then placing it on a carbon-plated copper mesh, the diameter of the core Si nanowire in a randomly selected coaxial nanowire ranges from 50 to 100 nm. The thickness of the coated Sb_2S_3 shell increased with the number of CBD cycles. It increased from 20 to 225 nm when the number of CBD cycles increased from 1 to 4.

3.3. Photoelectric Conversion Efficiency Measurement. The current-voltage (*I-V*) curves and photoelectric conversion efficiencies for various DSSCs based on the QDs/Si coaxial nanowire array-based photoelectrodes synthesized with different numbers of CBD cycles are illustrated in Figure 9 and Table 3, respectively. The photoelectric conversion efficiency reaches the highest value of 0.253% with 3 CBD cycles. The corresponding short-circuit current density, open-circuit voltage, and fill factor are 5.19 mA/cm^2, 0.24 V, and 20.33%, respectively.

When the QDs were coated only one time, the amount of QDs deposited was not enough to fully cover the core Si nanowire; therefore the photoinduced current was relatively small. The amount of QDs deposited increased with an increase in the number of CBD cycles so that the coaxial structure gradually formed. Hence the photoinduced current, as well as the photoelectric conversion efficiency, was

Table 3: Photoelectric conversion efficiencies for various DSSCs based on the QDs/Si coaxial nanowire array-based photoelectrodes synthesized using different numbers of CBD cycles.

CBD cycles	J_{sc} (mA/cm^2)	V_{oc} (V)	FF (%)	η (%)
1	2.71	0.20	21.56	0.116
2	4.51	0.20	17.36	0.157
3	5.19	0.24	20.33	0.253
4	2.48	0.20	21.38	0.106
5	1.29	0.21	20.80	0.056

increased. However, when the number of CBD cycles was increased to four, an excessive amount of QDs was deposited on the surface of the Si nanowires. This excessively thick shell of QDs degraded the photon absorption and photoelectron migration.

Although the proposed QDs/Si coaxial nanowire array-based DSSC has the advantages of simplicity, low cost, and high mass production feasibility, the convex IV curve results in a small FF, about 20% in this work. Possible explanations for this include the following.

(1) Large Resistance. The resistance of the proposed DSSC was measured by impedance spectroscopy analysis to be 20 k–25 kΩ. Hence the current density could only reach 5.19 mA/cm^2, resulting in a relatively lower photoelectric conversion efficiency. Furthermore, the fill factor was not as good as that of a conventional TiO_2-based DSSC. The leakage of the electrolyte due to less than fully tight packaging may be the major cause.

(2) Reduced Illumination. Sunlight irradiates through both the counter electrode and the electrolyte to reach the photoelectrode, resulting in a degraded illumination of the DQs, which then affects the photoelectric conversion efficiency.

In our future work, we will use a thinner Si wafer or increasing the doping concentration to reduce the resistance of the photoelectrode and a gelatinous electrolyte to avoid possible electrolyte leakage.

4. Conclusion

The DSSC is considered to be a highly promising technology for low cost renewable energy. However, the mass production of DSSC is still limited by a number of factors, including the aging of dye during operation and the relatively narrow light spectrum of the photon absorption. In this study, we proposed a novel and simple QDSSC structure based on a QDs/Si coaxial nanowire array-based photoelectrode. We use two-stage MAE to fabricate the micro-nano hybrid structure on a silicon substrate. We then used CBD to deposit Sb_2S_3 QDs on the surface of each silicon nanowire to form the QD/Si coaxial nanowire array to replace the conventional dye/TiO_2/TCO photoelectrode. The quantum dot replaces dye as the light-absorbing material. Since the Si-based photoelectrode is opaque, we obtain illumination from the counter electrode. Experimental results illustrate

that the QD/Si coaxial nanorod array-based photoelectrode synthesized by three runs of Sb_2S_3 deposition provides the highest photoelectric conversion efficiency of 0.253%. The corresponding short-circuit current density, open-circuit voltage, and fill factor are 5.19 mA/cm^2, 0.24 V, and 20.33%, respectively.

Conflict of Interests

The authors declare that there is no conflict of interests regarding the publication of this paper.

Acknowledgment

The authors would like to offer their thanks to the National Science Council of Taiwan for their financial support of this research under Grant no. NSC-101-2212-E-005-022-MY3.

References

[1] M. Grätzel, "Recent advances in sensitized mesoscopic solar cells," *Accounts of Chemical Research*, vol. 42, no. 11, pp. 1788–1798, 2009.

[2] A. Yella, H.-W. Lee, H. N. Tsao et al., "Porphyrin-sensitized solar cells with cobalt (II/III)-based redox electrolyte exceed 12 percent efficiency," *Science*, vol. 334, no. 6056, pp. 629–634, 2011.

[3] C. H. Chang and Y. L. Lee, "Chemical bath deposition of CdS quantum dots onto mesoscopic TiO_2 films for application in quantum-dot-sensitized solar cells," *Applied Physics Letters*, vol. 91, no. 5, Article ID 053503, 2007.

[4] D. R. Baker and P. V. Kamat, "Photosensitization of TiO_2 nanostructures with CdS quantum dots: particulate versus tubular support architectures," *Advanced Functional Materials*, vol. 19, no. 5, pp. 805–811, 2009.

[5] Y.-L. Lee and Y.-S. Lo, "Highly efficient quantum-dot-sensitized solar cell based on co-sensitization of CdS/CdSe," *Advanced Functional Materials*, vol. 19, no. 4, pp. 604–609, 2009.

[6] A. Tubtimtae, K.-L. Wu, H.-Y. Tung, M.-W. Lee, and G. J. Wang, "Ag_2S quantum dot-sensitized solar cells," *Electrochemistry Communications*, vol. 12, no. 9, pp. 1158–1160, 2010.

[7] A. Tubtimtae, M.-W. Lee, and G.-J. Wang, "Ag_2Se quantum-dot sensitized solar cells for full solar spectrum light harvesting," *Journal of Power Sources*, vol. 196, no. 15, pp. 6603–6608, 2011.

[8] J.-H. Im, C.-R. Lee, J.-W. Lee, S.-W. Park, and N.-G. Park, "6.5% efficient perovskite quantum-dot-sensitized solar cell," *Nanoscale*, vol. 3, no. 10, pp. 4088–4093, 2011.

[9] A. Tubtimtae and M.-W. Lee, "Effects of passivation treatment on performance of CdS/CdSe quantum-dot co-sensitized solar cells," *Thin Solid Films*, vol. 526, pp. 225–230, 2012.

[10] M. Shalom, Z. Tachan, Y. Bouhadana, H.-N. Barad, and A. Zaban, "Illumination intensity-dependent electronic properties in quantum dot sensitized solar cells," *Journal of Physical Chemistry Letters*, vol. 2, no. 16, pp. 1998–2003, 2011.

[11] S. Buhbut, S. Itzhakov, I. Hod, D. Oron, and A. Zaban, "Photo-induced dipoles: a new method to convert photons into photovoltage in quantum dot sensitized solar cells," *Nano Letters*, vol. 13, no. 9, pp. 4456–4461, 2013.

[12] P. N. Kumar, S. Mandal, M. Deepa, A. K. Srivastava, and A. G. Joshi, "Functionalized graphite platelets and lead sulfide quantum dots enhance solar conversion capability of a titanium dioxide/cadmium sulfide assembly," *The Journal of Physical Chemistry C*, vol. 118, no. 33, pp. 18924–18937, 2014.

[13] V. Amoli, R. Tiwari, A. Dutta, A. Bhaumik, and A. K. Sinha, "Structurally stabilized organosilane-templated thermostable mesoporous titania," *ChemPhysChem*, vol. 15, no. 1, pp. 187–194, 2014.

[14] S.-P. Ng, X. Q. Lu, N. Ding, C.-M. L. Wu, and C.-S. Lee, "Plasmonic enhanced dye-sensitized solar cells with self-assembly gold-TiO_2@core-shell nanoislands," *Solar Energy*, vol. 99, pp. 115–125, 2014.

[15] C. M. Yang, M. H. Hon, and I. C. Leu, "Hierarchical ZnO nanostructures growth by aqueous solution process for dye-sensitized solar cells," *Journal of the Electrochemical Society*, vol. 159, no. 7, pp. H638–H643, 2012.

[16] W. Lee, S. K. Min, V. Dhas, S. B. Ogale, and S. H. Han, "Chemical bath deposition of CdS quantum dots on vertically aligned ZnO nanorods for quantum dots-sensitized solar cells," *Electrochemistry Communications*, vol. 11, no. 1, pp. 103–106, 2009.

[17] W.-S. Chang, C.-C. Wu, M.-S. Jeng, K.-W. Cheng, C.-M. Huang, and T.-C. Lee, "Ternary Ag-In-S polycrystalline films deposited using chemical bath deposition for photoelectrochemical applications," *Materials Chemistry and Physics*, vol. 120, no. 2-3, pp. 307–312, 2010.

[18] Q. Guo, G. M. Ford, W.-C. Yang et al., "Fabrication of 7.2% efficient CZTSSe solar cells using CZTS nanocrystals," *Journal of the American Chemical Society*, vol. 132, no. 49, pp. 17384–17386, 2010.

[19] H. Morinaga, M. Suyama, and T. Ohmi, "Mechanism of metallic particle growth and metal-induced pitting on Si wafer surface in wet chemical processing," *Journal of the Electrochemical Society*, vol. 141, no. 10, pp. 2834–2841, 1994.

[20] J. S. Kim, H. Morita, J. D. Joo, and T. Ohmi, "The role of metal induced oxidation for copper deposition on silicon surface," *Journal of the Electrochemical Society*, vol. 144, no. 9, pp. 3275–3283, 1997.

[21] K. Peng and J. Zhu, "Morphological selection of electroless metal deposits on silicon in aqueous fluoride solution," *Electrochimica Acta*, vol. 49, no. 16, pp. 2563–2568, 2004.

[22] H. C. Liu and G. J. Wang, "Superior antireflection coating for a silicon cell with a micronanohybrid structure," *International Journal of Photoenergy*, vol. 2014, Article ID 807812, 8 pages, 2014.

[23] H. C. Liu and G. J. Wang, "Fabrication of high anti-reflection nanowires on silicon using two-stage metal-assisted etching," *Journal of Renewable and Sustainable Energy*, vol. 5, no. 5, Article ID 053115, 2013.